energies

MDPI

Article

New Thermochemical Salt Hydrate System for Energy Storage in Buildings

Yana Galazutdinova [1], Ruby-Jean Clark [1], Said Al-Hallaj [1], Sumanjeet Kaur [2] and Mohammed Farid [3,*]

[1] NETenergy LLC, Chicago, IL 60615, USA; yana@netenergytes.com (Y.G.); ruby-jean.clark@phasefoam.com (R.-J.C.); said@netenergytes.com (S.A.-H.)
[2] Lawrence Berkeley National Laboratory, Berkeley, CA 94720, USA; skaur1@lbl.gov
[3] Department of Chemical and Materials Engineering, University of Auckland, Auckland 1010, New Zealand
* Correspondence: m.farid@auckland.ac.nz

Abstract: This paper introduces an innovative design for an "inorganic salt-expanded graphite" composite thermochemical system. The storage unit is made of a perforated, compressed, expanded graphite block impregnated with molten $CaCl_2 \cdot 6H_2O$; the humid air passes through the holes that allow the moisture to diffuse and react with the salt. The prepared block underwent 90 hydration-dehydration cycles. Although most of the performed cycles were carried out with salt overhydration and deliquescence, the treated samples have remained mechanically and thermally stable with no drop in energy density. The volumetric energy density of the composite ranged from 135.5 to 277.6 kWh/m^3, depending on airflow rate and absolute humidity. To ensure composite material cycling stability, the energy density of the block was measured during hydration at similar conditions of absolute humidity, inlet temperature, and airflow rate (0.01 kg_{water}/kg_{air}, 20 °C, 400 l/min). The average energy density at these conditions was sustained at 219 kWh/m^3. The block integrity was monitored by visual inspection after removing it from the reactor chamber every few cycles. Both the composite material and its manufacturing process are simple and easy to scale up for future commercialization.

Keywords: thermochemical energy storage; salt hydrate; expanded graphite; calcium chloride; energy density; thermal efficiency

Citation: Galazutdinova, Y.; Clark, R.-J.; Al-Hallaj, S.; Kaur, S.; Farid, M. New Thermochemical Salt Hydrate System for Energy Storage in Buildings. *Energies* **2024**, *17*, 5228. https://doi.org/10.3390/en17205228

Academic Editor: Abdul-Ghani Olabi

Received: 13 September 2024
Revised: 14 October 2024
Accepted: 16 October 2024
Published: 21 October 2024

1. Introduction

Thermal energy storage (TES) plays an important role in the decarbonization of future energy systems. Specifically, the use of TES systems in the building and industrial sectors demonstrated high potential for energy conservation. It is well known that there are the following three methods of TES: sensible, latent, and thermochemical energy storage. Sensible heat storage consists of applying a temperature gradient to a media to store heat and release it at a later period. This method uses the thermal mass of building materials to enhance energy efficiency and thermal comfort [1]. The main disadvantage of this method is low energy density. Latent heat uses phase change materials (PCM) to store or release heat during a phase change. The use of latent heat storage in the building sector, such as peak shaving or increase of energy efficiency in HVAC systems, has been widely investigated by different researchers [2–4].

Thermochemical energy storage (TCES) has attracted significant attention in recent years due to its high energy density and suitability for long-term energy storage. Despite these advantages, TCES technologies are still in the early stages of development. A key component of the thermochemical heat storage system is the reactor, where heat and mass transfer, as well as chemical reactions, take place. Therefore, the current TCES literature focuses on the numerical and experimental investigation of different thermochemical reactor designs and concepts, TCES materials, and systems [5–8].

Concerning system configuration, TCES systems can be divided into open and closed systems. Open systems work at atmospheric pressure in contact with the environment, while closed systems work with pure vapor circulating in hermetically closed loops. A closed system is usually based on a sorption reactor (heat exchanger), a condenser, and an evaporator, which makes it more complex. An open system can be directly connected to ambient air where the moisture for the sorption process is captured [9].

As for the reactor configuration, packed bed, moving bed, and fluidized bed are the three main investigated reactor bed designs [10]. Packed bed reactors are a low-cost solution and the simplest technology compared to other types of reactors [11], which makes them an appropriate candidate for technology upscaling and integration. They are easy to build and operate. However, their main drawback is the pressure drop across the bed, which may compromise the power and energy output [12]. Another important disadvantage is the poor heat and mass transfer within the porous bed caused by low effective thermal conductivity and moisture diffusivity.

The composite material in the case of thermochemical packed bed reactors is subjected to different stresses, namely, chemical, mechanical, and thermal stresses. The volume changes due to moisture adsorption, thermal expansion/shrinkage, and pore size reduction may create pressure buildup during the gas release in solid-gas thermochemical materials. As a result, composite materials can crack, or their surface can be eroded, resulting in fines and reallocation of smaller particles. Considering the cycling operation nature of the TCES systems and the long life expectancy, it can lead to a significant increase in the pressure drop or to the collapse of the composite material [13].

There have been several investigations into open, packed bed thermochemical energy storage reactors. Namely, Zhang et al. [14] experimentally studied a 1 kWh lab-scale open sorption prototype reactor to store low-temperature heat for space heating. Activated alumina/LiCl composite material was employed to obtain high volumetric storage density. The authors stated that the investigated prototype can fulfill the space heating requirement with a system efficiency of 85–97%. They concluded that air higher than 30 °C can be provided over 7 h, corresponding to a volumetric storage density of 191 kWh/m^3. To confirm mechanical strength and structural stability, ten repeated simulative charging-discharging cycles were conducted without significant changes occurring.

An open thermochemical system was investigated by Michel et al. [10]. The work was conducted through the following two experimental setups: a small bench for mass transfer characterization and a prototype at a larger scale, using $SrBr_2/H_2O$ as a reactive pair. Analyzing mass transfer through the reactive bed, it was demonstrated that the reactive bed permeability changed during the reaction. Based on the experimental results, the permeability changed by one order of magnitude with the reactive bed density (from 10^{-9} to 10^{-12} m^2 when density ranges from 300 to 600 kWh/m^3). Thus, the thermochemical reaction led to significant local changes in the reactive bed properties. These changes need to be considered when designing and modeling fixed-bed thermochemical reactors [10]. Clark et al. [15] studied $SrCl_2 \cdot 6H_2O$ and cement-based composites and compared them with the well-researched zeolite 13X. The authors demonstrated that the salt combined with cement is promising since the cement prevented salt agglomeration. Furthermore, $SrCl_2$-cement could be dehydrated below 90 °C, while for zeolite dehydration, the temperature was 150 °C. Using an open lab-scale packed bed reactor, it was shown that the average volumetric energy storage density of $SrCl_2$ in cement (50 wt.%) and zeolite 13X materials was 136 kWh/m^3 and 164 kWh/m^3, respectively. The TCES materials were cycled at least five times with no decrease in volumetric energy density [15].

An ettringite-based material was investigated at the micro-scale and reactor-scale (using a new open-mode fixed-bed design) by Chen et al. [12]. The dehydration temperature of ettringite in the reactor was observed at 55–65 °C. For hydration, higher relative humidity resulted in higher energy and higher maximal specific power. The best reported volumetric energy storage density on system level was 104 kWh/m^3. Therefore, it was concluded that to improve the energy density and hydration kinetics, the porosity or ettringite content

needs to be increased [12]. Courbon et al. [16] synthesized four different LiBr-based composite materials with silica gel or activated carbon as a host porous matrix. The composite with 53 wt.% LiBr and silica gel demonstrated the most promising results with an energy storage density of 261 kWh/m^3 (hydration temperature: 30 °C, dehydration temperature: 80 °C, and water vapor pressure: 12.5 mbar) and 381 kWh/m^3 when the dehydration temperature was raised to 120 °C. However, when tested in a laboratory open-type reactor, the energy storage density decreased to 160–175 kWh/m^3 [16].

The heat storage performance of composite sorbents based on silica, polyethylene glycol (PEG), and calcium chloride was investigated in a lab-scale open fixed-bed reactor. The silica/PEG matrix managed to stabilize hydrated calcium chloride when the salt content was equal to 32 wt.% despite partial salt deliquescence. With a regeneration temperature of 130 °C, the best-performing composite sorbent exhibited an energy density of 154 kWh/m^3 over four successive sorption cycles at 30 °C and 42% relative humidity [17]. Gbenou et al. conducted a review of the characteristics of thermochemical energy storage (TCES) reactors for temperatures below 125 °C at microscopic and macroscopic levels. The authors outlined the main issues of TCES system-level studies, including the heat and mass transfer dilemma [18].

To the best of our knowledge, there are no studies on salt-hydrate-based thermochemical reactors that demonstrate a large number of cycles in a lab-scale, open reactor. The highest number found in the literature is twenty-five [19]. Most attempts for extensive cycling of TCES materials remain only on the material level using TGA-DSC, which does not provide a fair assessment of heat and mass transfer on a real scale. It should also be noted that many authors who reported very high energy density have based it on material volume rather than reactor or system. Therefore, this paper aims to address some of the above-mentioned shortcomings by considering both hydration and dehydration reactions and performing a high number of cycles in a laboratory-scale thermochemical reactor that was designed and assembled specifically for this purpose.

Calcium chloride hexahydrate ($CaCl_2 \cdot 6H_2O$) was chosen as a TCES material because of its safety, cycling stability, low cost, and suitable theoretical energy density [20–22]. Although expanded graphite (EG) was investigated as a porous host structure, no works have reached the system energy density threshold of 150 kWh/m^3 to become economically viable [23]. This limitation is associated with the selected design, which will be the focus of this paper. The thermal conductivity of the expanded graphite is extremely high and can vary from 140–500 W/(m·K) into the plane of the sheet while having a 3–10 W/(m·K) range in the perpendicular. This high thermal conductivity aims to improve heat transfer. To achieve structural stability, the EG flakes were compressed to form an expanded graphite matrix of a certain density [24].

This paper introduces an innovative approach to the "salt-EG" composite material manufacturing and design, providing a robust mechanical structure, excellent heat transfer, and moisture diffusion while maintaining the low-pressure drop required by any HVAC system. The prepared composite material underwent 90 hydration-dehydration cycles, which, to the best of our knowledge, has not been reported in the literature [25–27]. Moreover, the material remained stable with high energy density, although most performed cycles were carried out with $CaCl_2$ overhydration and deliquescence.

2. Materials and Methods

2.1. Thermogravimetric Analysis of the Salt and Composite

Thermogravimetric analysis was performed using TGA Q5000 (TA Instruments, New Castle, DE, USA). The measurements were performed in the standard platinum pan (100 µL), in a range from room temperature to 300 °C. Both pure $CaCl_2 \cdot 6H_2O$ and the composite with EG were tested with a heating rate of 1 °C/min.

2.2. Sample Preparation

The EG flakes were compacted to form an EG block with a 100 kg/m^3 density. Our goal was to maintain the minimal diffusion path without risking the mechanical stability of the material. Thus, a perforated block with a 3 mm spacing between the holes and a pitch distance of 8 mm was designed and machined using the Tormach 1100M CNC mill (Tormach, Madison, WI, USA) (see Figure 1).

Figure 1. Perforated EG block of novel design.

The pre-drilled perforated EG blocks were submerged into molten $CaCl_2 \cdot 6H_2O$ (Sigma Aldrich, 98% purity, CAS no. 774-34-7, St. Louis, MO, USA) for 72 h and then dried in a Quincy Lab 20GC oven (Burr Ridge, IL, USA) at 150 °C. The composite salt content was determined gravimetrically from the weights of the EG before and after impregnation and drying. The parameters of the perforated blocks after soaking and drying are shown in Table 1. The composite Block 1 was cycled in the thermal chamber as a proof of concept, while composite Block 2 was cycled in the TCM reactor.

Table 1. Parameters of the composite perforated blocks after soaking and drying. Please note that Block 1 was cycled in the thermal chamber, while Block 2 was cycled in the reactor.

Sample	Impregnation Type	Sample Dimensions, [mm]	EG Density, [kg/m^3]	Anhydrous Salt Content, [wt.%]	Perforated Block Volume (Solid), [m^3]	Perforated Block Volume (Total), [m^3]
Block 1	molten	117 × 75 × 75	100	62	0.00047	0.000655
Block 2	molten	275 × 120 × 73	100	63	0.00171	0.00241

2.3. Thermochemical Reactor Design and Construction

To examine the performance of the manufactured perforated block containing $CaCl_2 \cdot 6H_2O$, a lab-scale open reactor was designed and built. Figure 2 demonstrates the assembled TCM reactor setup. The air from a compressed air system enters the setup through an airflow meter, passes through a heater (Cool Touch™ 150 Heat Torch, Arden, NC, USA), and a humidifier (PermaPure FC150-480, Lakewood, NJ, USA), and enters the reactor chamber. The humidifier is connected to a water circulator (Julabo F32-ME, Allentown, PA, USA) that pumps deionized water through the humidifier to humidify the air. The humidity is controlled by adjusting the water flowmeter and two-way valves at the entrance of the humidifier and the direct line from the compressed air system. During dehydration, air is heated using the in-line air heater and is not passed through the humidifier. During hydration, the heater is turned off, and air is passed through the humidifier.

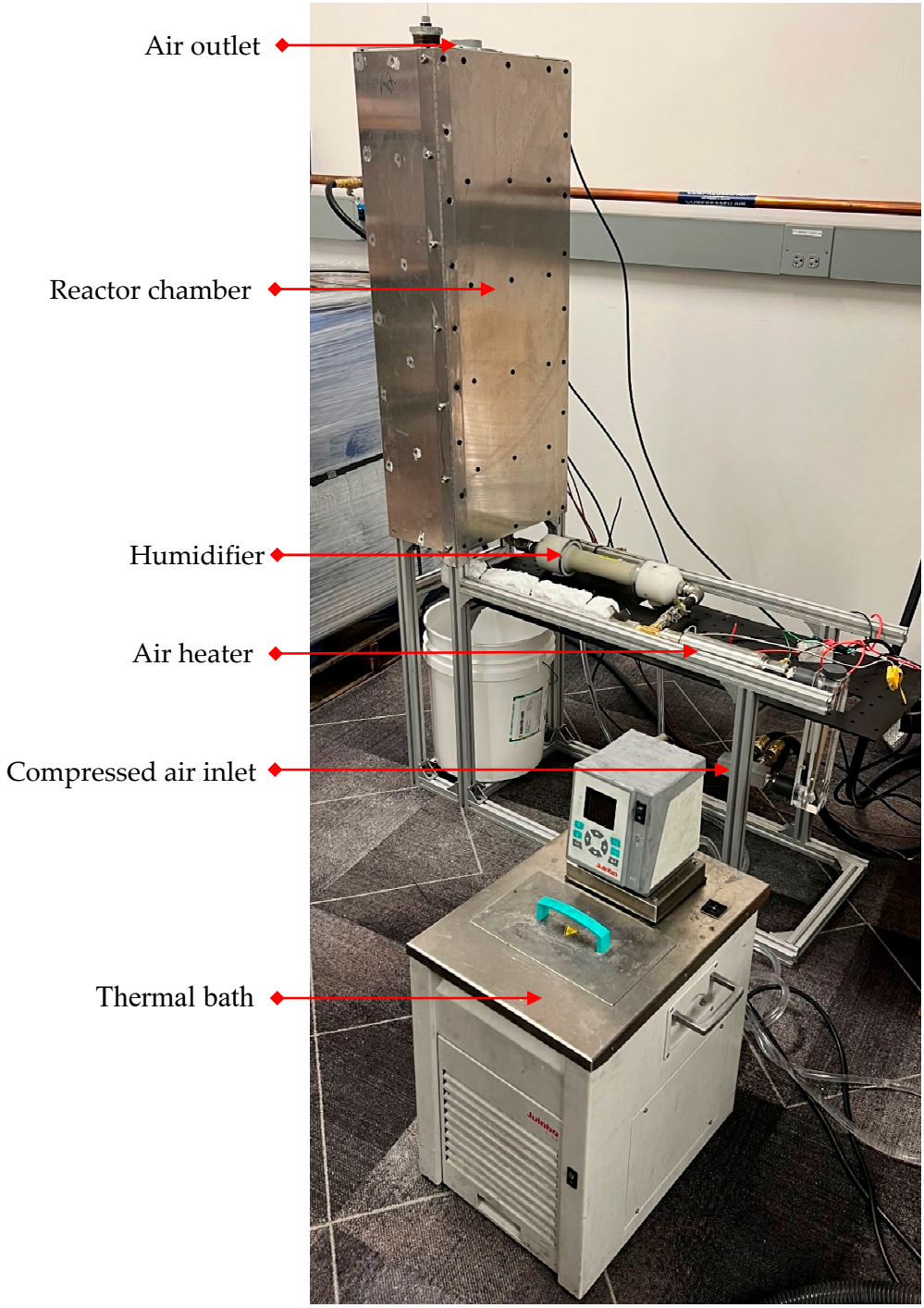

Figure 2. Assembled TCM reactor components.

The humidity and temperature sensors (Rotronic HC2 screw-in probe (Bassersdorf, Switzerland) with temperature accuracy of ±0.1 °C and relative humidity accuracy of ±0.8% RH, Pico Technology Type T thermocouple (St. Neots, UK) with accuracy of ±0.5 °C) were placed at the inlet, in the middle and at the outlet of the reactor chamber.

The reactor chamber (see Figure 3) contains four compartments that are insulated with two types of insulation: the first layer is a ceramic fiber (white) that minimizes heat losses from the system; the second layer (yellow) is a high-temperature polyimide foam that prevents the composite material damage due to its expansion during cycling. Moreover, the reactor chamber was wrapped with a 1" thick ceramic fiber blanket that serves as a third layer of insulation (not shown in Figure 3). Each compartment accommodates one

block of the composite material. This study focuses on single block measurements; the other compartments were left for future work.

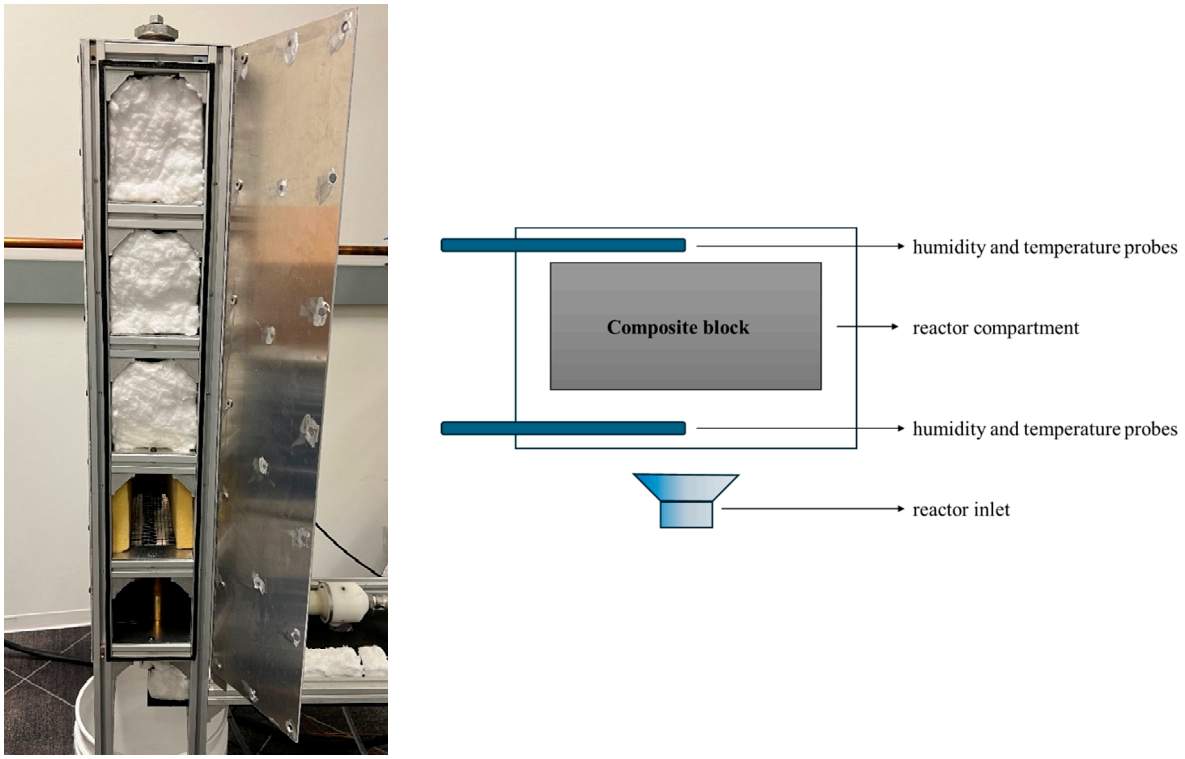

Figure 3. The TCM reactor chamber.

The studied block underwent ninety hydration/dehydration cycles, which were carried out at different conditions of relative humidity, inlet temperature, and airflow rate. The temperature and humidity measurements were recorded every 5 s. The block was dehydrated until the absolute humidities of the inlet and outlet were equal, and then the reactor was allowed to cool before starting the hydration. It should be indicated that the reactor and the block were cooled down with compressed air at room temperature and with an average relative humidity of 12–14% for approximately four hours. The average dehydration time and temperature were 4 h and 150 °C, respectively. This temperature was chosen to accelerate the dehydration time. The hydration reactions were performed overnight, with an average reaction time of 16 h and a range of relative humidity between 12–80%.

2.4. Energy Analysis

2.4.1. Analysis of the Environmental Chamber

The volumetric energy density (kWh/m^3) for Block 1 cycled in the environmental chamber was calculated based on the water uptake in the following:

$$Q_v = \frac{\Delta m_{H2O} \Delta h_r}{V_{com}} \quad (1)$$

where, Δm_{H2O} is the mass of water gained by the sample, Δh_r is the enthalpy of the reaction, and V_{com} is the volume of the block. The full enthalpy of the reaction Δh_r of solid $CaCl_2$ and water vapor (3200 kJ/kg$_{water}$) was calculated from [28].

2.4.2. Analysis for the Reactor

Hydration Reaction

During the hydration reaction, water vapor reacts with $CaCl_2$ in the graphite block exothermically. The released heat is used to heat both the air and the reactor. The energy balance for the hydration reaction is as follows:

$$Q_{recovered} + Q_{sensible} + Q_{loss} = Q_{reaction} \quad (2)$$

where $Q_{recovered}$ is the energy recovered by the outlet air, $Q_{sensible}$ is the sensible heating of the composite material and the reactor, Q_{loss} refers to the heat losses to ambient, and $Q_{reaction}$ refers to the overall heat of the reaction between the salt and water vapor. The units of these terms are kW/m^3. The calculation of $Q_{recovered}$ is shown in the following equation [29,30]:

$$Q_{recovered} = \frac{\dot{V}_a(T_{out} - T_{in})(C_{p\ air} + C_{p\ water\ vapor}\left(\frac{\chi_{in}+\chi_{out}}{2}\right))}{\nu_{da} \cdot V_{com}} \quad (3)$$

where $\dot{V}_a$ refers to the volumetric flow rate of the inlet air, ν_{da} refers to the specific volume of the inlet dry air, and V_{com} refers to the volume of the composite material. It should be noted that two types of V_{com} are used throughout this paper. One refers to only the volume of solid material, and the other considers the volume of the cavity required for air to pass through the block. These are referred to as material and reactor volumes, respectively. T_{out} and T_{in} refer to the outlet and inlet air temperatures and χ is the absolute humidity of the inlet or outlet air.

The sensible heating of the composite material and the reactor is calculated from the following equation:

$$Q_{sensible} = \frac{m_{com} Cp_{com}(T_{com\ 2} - T_{com\ 1})}{V_{com}} \quad (4)$$

where m_{com} is the mass of composite material, $C_{p\ com}$ is the heat capacity of the composite material, $T_{com\ 1}$ and $T_{com\ 2}$ are the initial and final temperatures of the composite material, respectively.

The heat losses to the surroundings are calculated from in the following equation:

$$Q_{loss} = \frac{UA(\frac{T_{in}+T_{out}}{2} - T_{amb})}{V_{com}} \quad (5)$$

where the coefficient UA = 0.000106 kW/K was calculated through experimental work. This was performed by running dry air at 100 °C through an empty reactor and calculating the difference in temperature between the inlet and outlet air flows at a steady state (Equation (6) as follows):

$$UA = \frac{\frac{\dot{V}_a}{\nu_{da}}\ Cp_{com}(T_{out} - T_{in})}{\frac{T_{in}+T_{out}}{2} - T_{amb}} \quad (6)$$

The theoretical value was also calculated through Equation (7) and the resulting value was UA = 0.000155 kW/K, which is in good agreement with the experimental value.

$$UA = \frac{1}{\frac{\Delta x_1}{k_1} + \frac{\Delta x_2}{k_2} + \frac{\Delta x_3}{k_3}} \times L \times h \quad (7)$$

where Δx_1, Δx_2, Δx_3, and k_1, k_2, k_3 are the insulation layers thicknesses and thermal conductivities, respectively, h is the height of the block, and L is the outer perimeter of the reactor.

It should be noted that due to the absence of a temperature sensor in the block, the temperature is taken as an average between the inlet and the outlet temperature.

Dehydration Reaction

During the dehydration reaction, dry, hot air passes through the reactor, removing moisture from the composite block (endothermic process). The energy balance for the dehydration reaction is as follows:

$$Q_{input} - Q_{sensible} - Q_{loss} = Q_{reaction} \quad (8)$$

where Q_{input} is the net energy input into the system during dehydration, $Q_{sensible}$ is sensible heating of the material and the reactor (calculated from Equation (4)), Q_{loss} represents heat losses to the surroundings (calculated from Equation (5)), and $Q_{reaction}$ is the heat of dehydration reaction. Q_{input} can be calculated from the following equation:

$$Q_{input} = \frac{\dot{V}_a(T_{in} - T_{out})(C_{p\ air} + C_{p\ water\ vapor}\left(\frac{\chi_{in}+\chi_{out}}{2}\right))}{\nu_{da} \cdot V_{com}} \quad (9)$$

Total Balance

The total volumetric energy density includes the heat recovered by the air in case of hydration, the energy input into the system in case of dehydration, the sensible heating of the reactor, and heat losses to the surroundings over the entire period of the reaction. The volumetric energy density can be calculated via integration over the entire reaction period as follows:

$$E_{tot}(hydration) = \int_0^{16} (Q_{recovered})dt + \int_0^{16} (Q_{sensible\ hydr})dt + \int_0^{16} \left(Q_{loss\ hydr}\right)dt \quad (10)$$

$$E_{tot}(dehydration) = \int_0^{4} (Q_{input})dt - \int_0^{4} (Q_{sensible\ hydr})dt - \int_0^{4} (Q_{loss\ hydr}\ )dt \quad (11)$$

The overall thermal efficiency is shown in Equation (12):

$$\eta = \frac{E_{tot}(hydration)}{E_{tot}(dehydration)} \quad (12)$$

3. Results and Discussion

3.1. Thermogravimetric Analysis of the Salt and Composite

TGA was used to analyze the dehydration behavior of both composite material and pure salt, as shown in Figure 4. The total mass loss for pure $CaCl_2 \cdot 6H_2O$ is 49.4 wt.%, corresponding to full dehydration of 6 moles of water. The same can be said for composite EG-salt material with a total mass loss of 39.6 wt.%, corresponding to 6 moles of water.

As can be seen from Figure 4 the TGA indicates that the expanded graphite composite shows dehydration at lower temperature, due to the improved heat transfer caused by the graphite matrix with high thermal conductivity [31]. The mass of both samples was similar to ensure adequate comparison. This suggests that the addition of EG will improve thermal efficiencies when compared to pure salt.

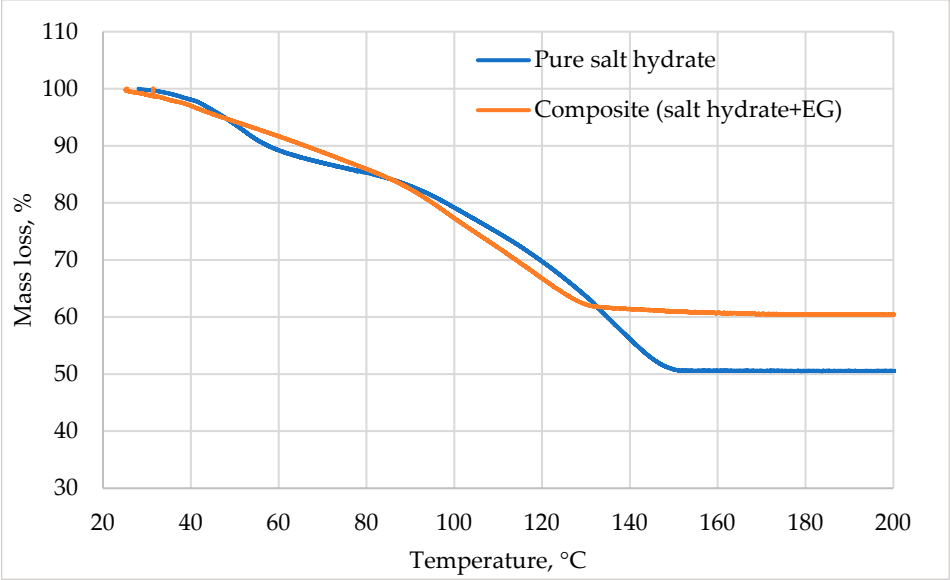

Figure 4. Thermogravimetric analysis for pure $CaCl_2 \cdot 6H_2O$ and composite $CaCl_2 \cdot 6H_2O$-EG sample.

3.2. Composite Block Cycling in the Environmental Test Chamber

The cycling of the perforated Block 1 was performed in the Thermotron SE-400-6-6 Environmental Test Chamber; the dehydration reactions were performed in a Quincy Lab 20GC oven. The cycling protocol was the following:

1. Hydration reaction at 20 °C and 40% RH for 17 h;
2. Dehydration reaction at 150 °C overnight;
3. Repeat.

The energy density of the perforated composite block for certain cycles is presented in Table 2. The block showed excellent structural stability with no signs of degradation (Figure 5), with the material energy density between 137 and 161 kWh/m^3 and the reactor (total volume of the block using bulk density) energy density between 97 and 114 kWh/m^3.

Table 2. Composite $CaCl_2$/EG perforated block energy density throughout the cycling in the environmental chamber.

Cycle	Energy Density per Solid Volume (Material Level), [kWh/m^3]	Energy Density per Volume (Reactor Level), [kWh/m^3]
2	154.9	110.1
6	136.5	97.0
10	160.6	114.1

Since the initial testing of the perforated composite block performed in the environmental chamber was promising and demonstrated satisfactory results, it was decided to take it to the next stage and perform extensive cycling in the TCM reactor.

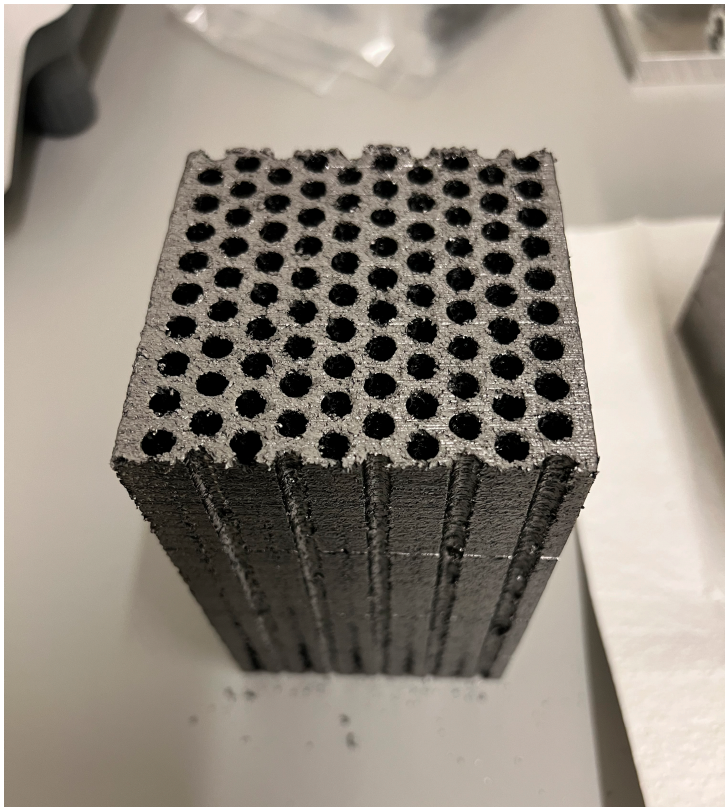

Figure 5. Perforated composite EG block after ten cycles in the environmental chamber.

3.3. Composite Block Cycling in the Reactor

The perforated block was cycled over 90 hydration-dehydration cycles. The energy density of the block was monitored through hydration reactions performed at similar conditions of inlet absolute humidity, temperature, and airflow rate. The block integrity was checked by visual inspection after removing it from the reactor. The energy density used for comparison was volume-based rather than mass-based, which is needed in the design of any storage unit (Table 3). Both maximum theoretical energy density values are derived from the full hydration reaction and formation of the solid salt, $CaCl_2 \cdot 6H_2O$.

Table 3. Parameters of the composite $CaCl_2$/EG perforated block.

Sample	Anhydrous Salt Content [wt.%]	Mass of Anhydrous Salt, [kg]	Mass of Water Required for the Formation of Solid Salt, [kg]	Theoretical Heat of Reaction, [kJ/kg_{water}]	Max Theoretical Energy Density (Material Level), [kWh/m^3]	Max Theoretical Energy Density (Reactor Level), [kWh/m^3]
Block 2	62.9	0.3697	0.3595	3200 [28]	186.9	132.6

During the cycling of the composite block in the TCM reactor, we evaluated the effect of the airflow rate, relative humidity, and inlet temperature on the energy density, power density, and temperature lift, as described in the following sections.

3.3.1. Effect of the Airflow Rate

The energy density should be independent of the airflow rate. However, Figure 6 shows an increase in energy density (ranging from 172.9 to 277.5 kWh/m^3) as the airflow rate increases. The higher flow rates are expected to increase heat and mass transfer rates, but the main reason for high energy density is the fact that the humidity is sustained throughout the reaction bed at high airflow rates. If the air is left on for longer periods, the block should have similar energy density at the various flow rates.

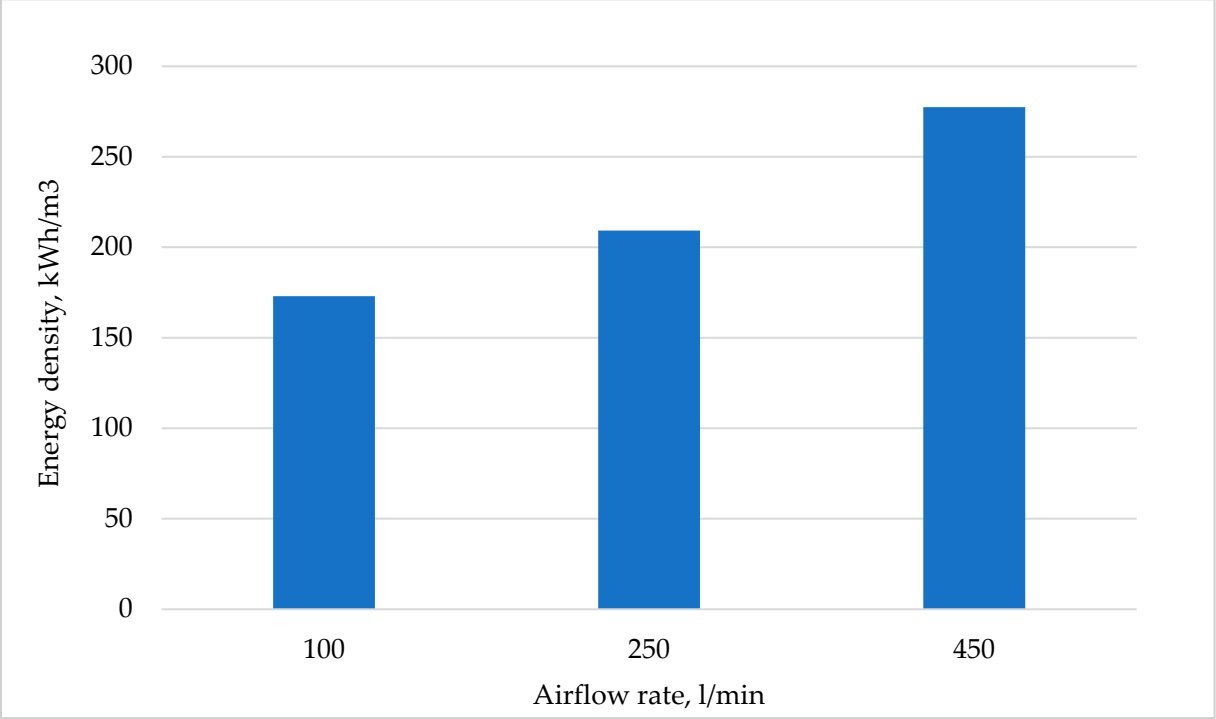

Figure 6. The energy density of the composite $CaCl_2$/EG perforated block at different airflow rates over a period of 16 h and inlet conditions of 65% RH and 21 °C.

The temperature lift dependence on the airflow rate is demonstrated in Figure 7. The lower airflow rate corresponds to the higher temperature increase as they are inversely proportional (see Equation (3)).

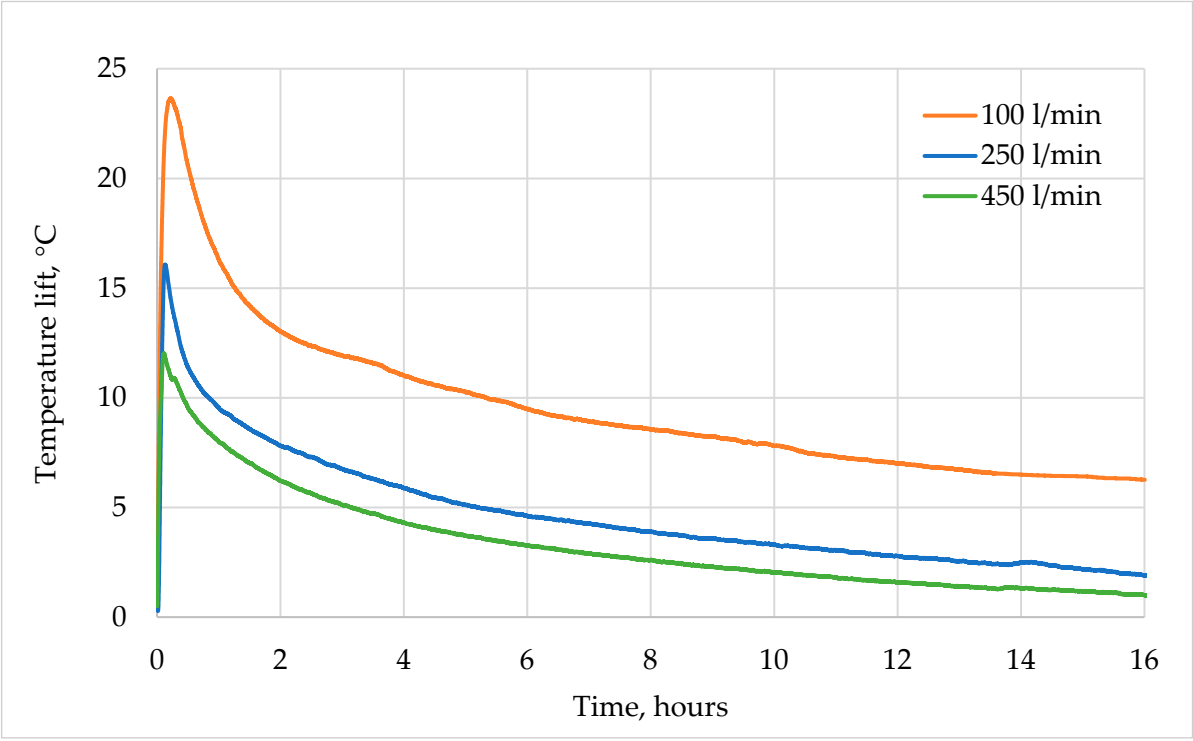

Figure 7. Temperature lift of the composite $CaCl_2$/EG perforated block at different airflow rates and the same inlet conditions of 65% RH and 21 °C.

The increase in the instantaneous power output at higher flow rates in Figure 8 is anticipated since the power is a function of airflow rate (Equation (3)); this was also demonstrated by other authors for other materials and systems [14,15,32,33].

The temperature lift and power density are high during the first few hours but decline for the remaining period. The hydration reaction of $CaCl_2$ does not take place in a single step and has several equilibrium states [34]. The rapid increase in outlet temperature is due to the reaction of 1 and 2 moles of water, which is known to be very fast even at low humidity and occurs over the whole body of the graphite block. This is in contrast to the reaction from 2 to 6 moles, which is slower and occurs only at the inlet section of the reactor, progressing to other parts of the block gradually as a sharp reaction front [35].

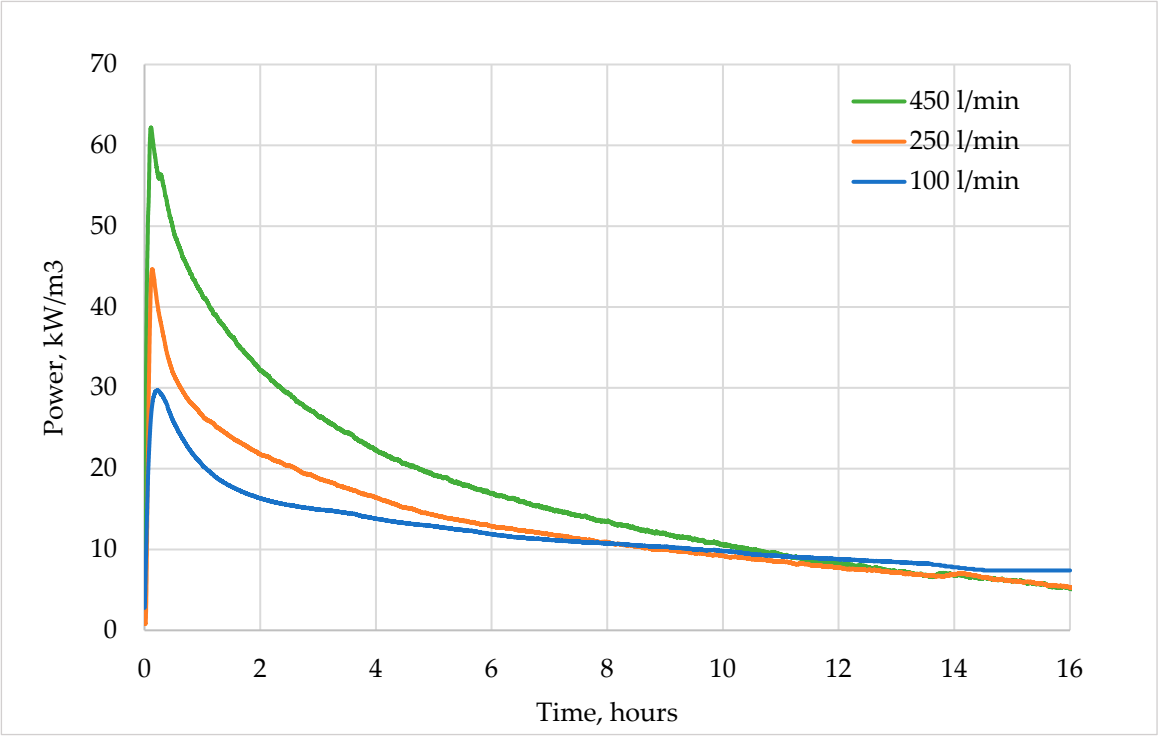

Figure 8. The power density of the composite $CaCl_2$/EG perforated block at different airflow rates and the same inlet conditions of 65% RH and 21 °C.

3.3.2. Effect of Relative Humidity

Increasing relative humidity shows a significant increase in the energy density of the block at the same airflow rate, from 50.2 to 244.4 kWh/m^3 (Figure 9), exceeding the maximum theoretical value due to $CaCl_2$ overhydration.

According to the equilibrium phase diagram of $CaCl_2$ and its hydrates, a full hydration reaction with the formation of $CaCl_2 \cdot 6H_2O$ occurs at very low relative humidity (20 °C and ~20% RH) [22]. However, in the case of composite materials, there is a significant mass transfer limitation, which slows down the reaction, especially at low RH [36]. At higher RH, there is a large driving force for hydration [37]. This increased driving force results in an increase in a temperature lift and hence the instantaneous power output, as shown in Figure 10.

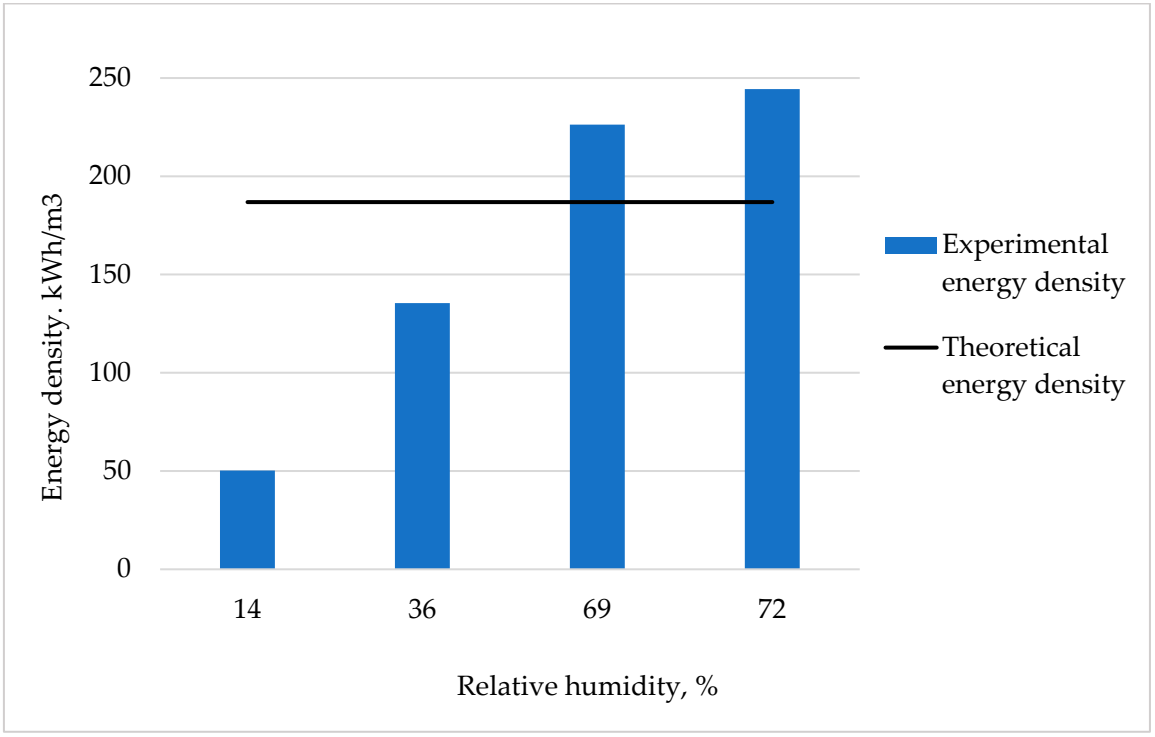

Figure 9. Effect of relative humidity on the energy density of the composite $CaCl_2$/EG perforated block over a period of 16 h and an airflow rate of 400 l/min.

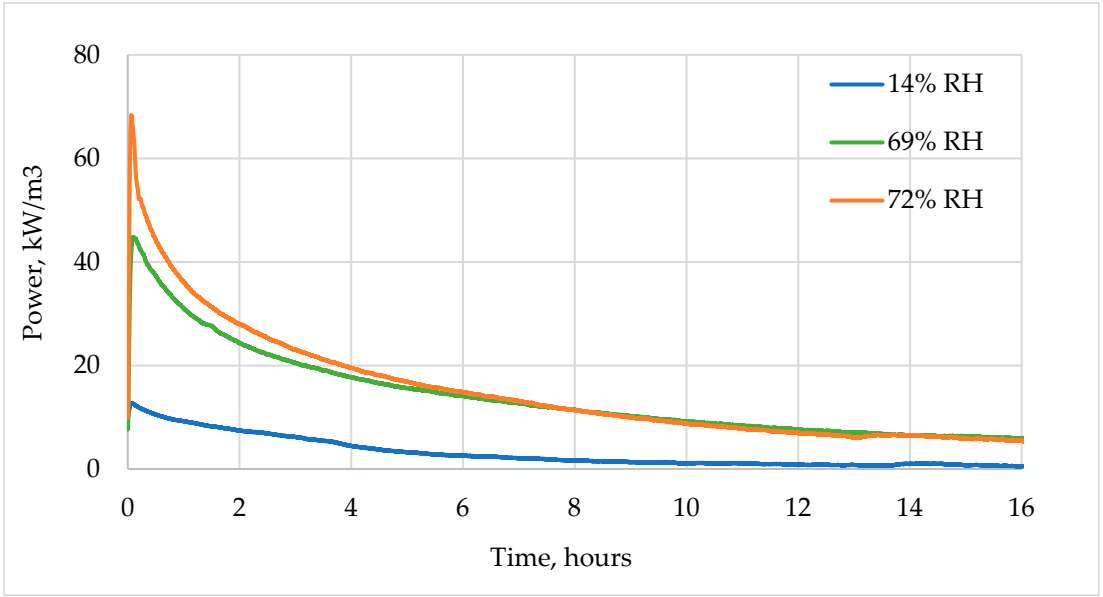

Figure 10. Effect of humidity power output of the composite $CaCl_2$/EG perforated block.

3.3.3. Cycling Performance

The composite block underwent 90 hydration-dehydration reactions. To ensure composite material cycling stability, the energy density of the block was measured during hydration at similar conditions of absolute humidity and air inlet temperature (see Table 4). The block integrity was also monitored by visual inspection after removing it from the reactor chamber every few cycles (see Figure 11).

Table 4. Composite $CaCl_2$/EG perforated block energy density throughout the cycling at an airflow rate of 400 l/min.

Cycle	Energy Density per Solid Volume (Material), [kWh/m^3]	Energy Density per Total Volume (Reactor), [kWh/m^3]	Absolute Humidity, [kg_{water}/kg_{air}]	Inlet Temperature, [°C]
6	205.1	144.8	0.009	19
15	212.5	150.0	0.010	20
23	222.8	157.3	0.009	18
31	220.3	155.5	0.010	19
45	228.2	161.1	0.010	22
52	224.7	158.7	0.010	21
60	217.5	153.5	0.010	22
69	209.7	148.1	0.009	20
76	222.5	157.1	0.011	21
84	226.3	159.8	0.010	20
Average	219.0 ± 2.3	154.6 ± 1.6	0.010 ± 0.0002	20 ± 0.4

As can be seen from Table 4, the energy density of the block did not change significantly during cycling, which indicates excellent stability of the composite material even after 90 hydration-dehydration cycles. The average energy density of the composite material at the indicated conditions is 219 kWh/m^3, which exceeds the maximum theoretical value of 186.9 kWh/m^3 (for 6 moles of H_2O). This is due to $CaCl_2$ overhydration and absorption of more than six moles of water per mole of salt. This high energy density corresponds to 154.6 kWh/m^3 based on the reactor volume.

Moreover, it should be indicated that following each dehydration, the block was cooled down with compressed air at room temperature, with an average relative humidity of 12–14% for approximately four hours. To estimate the amount of water reacting during the cooling period, we performed the hydration reaction by running "dry" air from the compressed air system through the block overnight without passing through the hydration unit. The total energy density generated after 16 h of such reaction was 55 kWh/m^3, while the energy density after 4 h (average cooling time) was 32 kWh/m^3. This approximately corresponds to the heat generated from the absorption of 2 and 1 moles of water, respectively.

Figure 11 shows photos of the composite block after each removal from the reactor chamber. The composite block demonstrated excellent mechanical stability even after 90 cycles, even though $CaCl_2$ was overhydrated and deliquesced. Some minor EG cracks formed due to $CaCl_2$ volume change during hydration-dehydration, however, those did not affect the overall material stability.

Figure 11. Composite $CaCl_2$/EG perforated block during cycling in the reactor.

3.4. Energy Density and Thermal Efficiency Analysis

This section contains the results of energy density and thermal efficiency analysis for the selected cycles with varying values of relative humidity, inlet temperature, and airflow rate, as aforementioned (see Table 5). The dehydration temperature was kept constant during the cycling. All values for energy density are calculated for the hydration reaction time of 16 h and the dehydration reaction time of 4 h.

Table 5. Energy density and thermal efficiency analysis.

Cycle	Absolute Humidity, [kg_{water}/kg_{air}]	Inlet Temperature, [°C]	Airflow Rate, [l/min]	Volumetric Energy Density (Material), [kWh/m^3]		Sensible Heat, [kWh/m^3]		Heat Loss, [kWh/m^3]		Thermal Efficiency
				H *	D **	H	D	H	D	
Effect of inlet temperature										
38	0.0062	23	400	135.5	202.2	0.2	16.7	1.9	23.7	0.8
36	0.0068	13	400	235.5	267.3	−1.3	17.1	−7.7	21.8	1.0
40	0.0075	14	400	242.3	285.9	−1.2	17.1	−5.9	23.1	1.0
Effect of relative humidity										
38	0.0062	23	400	135.5	202.2	0.2	16.7	1.9	23.7	0.8
18	0.0097	20	400	223.8	245.0	−0.2	9.9	−0.5	13.8	1.0
83	0.0100	20	400	230.2	286.8	−1.8	17.0	−1.7	22.1	0.9
77	0.0110	20	400	244.4	-	−0.5	-	−1.1	-	-
Effect of airflow rate										
1	0.0091	20	100	172.9	-	−0.4	-	1.9	-	-
21	0.0102	22	250	209.3	238.0	−1.6	17.3	0.6	23.6	1.0
25	0.0097	21	450	277.6	-	0.0	-	−0.2	-	-

* Hydration. ** Dehydration.

The thermal efficiency of the system varies in the range of 0.8–1.0 under various working conditions. When calculating thermal efficiency, we have assumed that heat loss through insulation and sensible heating can be recovered (Equation (12)). This is because the heat loss is large for a lab-scale reactor, but when scaling up to the industrial-scale reactor, the heat losses will be negligible. Also, in practice, dehydration can be followed by immediate hydration without cooling the reactor down, which allows recovery of the sensible heat.

Regarding the recovered volumetric energy density, the effect of inlet temperature, relative humidity, and airflow rate is compared. The energy density ranges from 135.5 to 277.6 kWh/m^3 for the material, which corresponds to 96.1–196.9 kWh/m^3 for the reactor. As already discussed, the energy density increases with a decrease in inlet temperature or an increase in absolute humidity. Also, there is a clear increase in the energy density as the airflow rate increases.

3.5. Comparison to the State of the Art

Table 6 shows a comparison of the studies that used an open, fixed-bed reactor. According to Courbon et al. [23], an energy storage density of 150 kWh/m^3 may be considered a minimum target value to ensure a breakthrough compared to sensible heat storage. Another crucial parameter for the long-life operation of the system is high cycling stability. Therefore, the developed composite $CaCl_2$/EG combines all desired characteristics, such as high energy density (196.9 kWh/m^3), stability even after 90 hydration-dehydration cycles, and low cost of the materials.

Table 6. Comparison of reactor performance for several composite thermochemical energy storage materials.

TCES Material	System	Reactor Energy Density, [kWh/m^3]	Number of Cycles	Cost per kg, [USD]	Reference
Ettringite	Open, fixed bed	56–104	-	-	[38]
LiBr (53 wt.%), silica gel	Open, fixed bed	160–175	10	-	[16]
$CaCl_2$ (32 wt.%), silica, PEG	Open, fixed bed	154	4	220	[17]
Zeolite 13X	Open, fixed bed	124	5	1.5	[39]
$SrCl_2{\cdot}6H_2O$ (50 wt.%), cement	Open, fixed bed, cascade	138	5	0.9	
$SrCl_2{\cdot}6H_2O$ (50 wt.%), cement	Open, fixed bed	132	7	0.3	
LiCl (14.7 wt.%), activated alumina	Open, fixed bed	191	10	-	[14]
$SrBr_2$	Open, fixed bed	203	7	-	[10]
$CaCl_2$ (22 wt.%), mesoporous ceramic honeycomb filter	Open, fixed bed	76	25	-	[19]
$CaCl_2$ (63 wt.%), EG	Open, fixed bed	197	90	0.6	Present work

4. Conclusions

This study introduced an innovative approach to the "salt-EG" composite material manufacturing and design, providing a robust mechanical structure, excellent heat transfer, and moisture diffusion while maintaining the low-pressure drop required by any HVAC system. The prepared composite material underwent 90 hydration-dehydration cycles, which, to the best of our knowledge, has not been reported in the literature. Moreover, the material remained stable with high energy density, although most performed cycles were carried out with $CaCl_2$ overhydration and deliquescence.

The volumetric energy density of the block ranged from 135.5 to 277.6 kWh/m^3 (from 96.1 to 196.9 kWh/m^3 based on true reactor volume) depending on the airflow and humidity conditions. The lower airflow rate demonstrated higher temperature lifts. On the other hand, an increase in air flow rate resulted in higher instantaneous power output and an increase in volumetric energy density.

To ensure composite material stability, the energy density of the block was measured every several cycles at similar conditions of absolute humidity, inlet temperature, and airflow rate (0.01 kg_{water}/kg_{air}, 20 °C, 400 l/min). The average material energy density at these conditions was stable at 219.0 kWh/m^3, corresponding to 154.6 kWh/m^3 based on reactor volume.

Author Contributions: Conceptualization, Y.G., R.-J.C. and M.F.; Methodology, Y.G. and R.-J.C.; Validation, Y.G.; Formal analysis, Y.G. and R.-J.C.; Investigation, Y.G.; Resources, S.K.; Data curation, Y.G.; Writing—original draft, Y.G.; Writing—review & editing, Y.G., R.-J.C., S.A.-H., S.K. and M.F.; Supervision, S.A.-H. and M.F.; Project administration, S.A.-H., S.K. and M.F.; Funding acquisition, S.A.-H. and S.K. All authors have read and agreed to the published version of the manuscript.

Funding: Funding for the project was provided through a grant to Lawrence Berkeley National Laboratory from the U.S. Department of Energy Office of Energy Efficiency and Renewable Energy Building Technologies Office for the provided funding. The views expressed in the article do not necessarily represent the views of the DOE or the U.S. Government. Lawrence Berkeley National Laboratory is operated by the University of California for the U.S. DOE under Contract No. DE-AC02-05CH11231. The corresponding author would like to acknowledge the support of both NetEnergy, USA, and the New Zealand Ministry of Business, Innovation, and Employment (MBIE)—(Project UOAX2211).

Data Availability Statement: The original contributions presented in the study are included in the article, further inquiries can be directed to the corresponding author.

Conflicts of Interest: Authors Yana Galazutdinova, Ruby-Jean Clark and Said Al-Hallaj were employed by the company NETenergy LLC. The remaining authors declare that the research was conducted in the absence of any commercial or financial relationships that could be construed as a potential conflict of interest.

Nomenclature

$Q_{recovered}$	Volumetric heat recovered, kW/m^3
$Q_{sensible}$	Volumetric sensible heat, kW/m^3
Q_{loss}	Volumetric heat loss, kW/m^3
Q_{input}	Volumetric heat input, kW/m^3
$Q_{reaction}$	Volumetric heat of reaction, kW/m^3
$\dot{V}_a$	Volumetric flow rate, m^3/s
v_{da}	Specific volume of dry air, m^3/kg
T	Temperature, K, °C
χ	Absolute humidity, kg_{water}/kg_{air}
V_{com}	Volume of material, m^3
m	Mass, kg
C_p	Specific heat capacity, kJ/kg·K
E_{tot}	Overall energy storage density, kWh/m^3
η	Thermal efficiency
UA	heat loss coefficient, kW/K
Indices	
in	Inlet air
out	Outlet air
amb	Ambient air
da	dry air
com	composite

References

1. Lind, J.; Möllerström, E.; Averfalk, H.; Ottermo, F. Energy flexibility using the thermal mass of residential buildings. *Energy Build.* **2023**, *301*, 113698. [CrossRef]
2. De Gracia, A.; Cabeza, L.F. Phase change materials and thermal energy storage for buildings. *Energy Build.* **2015**, *103*, 414–419. [CrossRef]
3. Candanedo, J.A.; Dehkordi, V.R.; Stylianou, M. Model-based predictive control of an ice storage device in a building cooling system. *Appl. Energy* **2013**, *111*, 1032–1045. [CrossRef]
4. Toffoletti, G.; Cortella, G.; D'Agaro, P. Thermodynamic and economic seasonal analysis of a transcritical CO_2 supermarket with HVAC supply through ice thermal energy storage (ITES). *J. Clean. Prod.* **2024**, *434*, 139832. [CrossRef]
5. Clark, R.J.; Mehrabadi, A.; Farid, M. State of the art on salt hydrate thermochemical energy storage systems for use in building applications. *J. Energy Storage* **2020**, *27*, 10114. [CrossRef]

6. Marín, P.E.; Milian, Y.; Ushak, S.; Cabeza, L.F.; Grágeda, M.; Shire, G.S.F. Lithium compounds for thermochemical energy storage: A state-of-the-art review and future trends. *Renew. Sustain. Energy Rev.* **2021**, *149*, 111381. [CrossRef]
7. Yan, T.; Zhang, H. A critical review of salt hydrates as thermochemical sorption heat storage materials: Thermophysical properties and reaction kinetics. *Sol. Energy* **2022**, *242*, 157–183. [CrossRef]
8. Tregambi, C.; Troiano, M.; Montagnaro, F.; Solimene, R.; Salatino, P. Fluidized Beds for Concentrated Solar Thermal Technologies—A Review. *Front. Energy Res.* **2021**, *9*, 618421. [CrossRef]
9. Farulla, G.A.; Cellura, M.; Guarino, F.; Ferraro, M. A review of thermochemical energy storage systems for power grid support. *Appl. Sci.* **2020**, *10*, 3142. [CrossRef]
10. Michel, B.; Mazet, N.; Neveu, P. Experimental investigation of an open thermochemical process operating with a hydrate salt for thermal storage of solar energy: Local reactive bed evolution. *Appl. Energy* **2016**, *180*, 234–244. [CrossRef]
11. Zsembinszki, G.; Sole, A.; Barreneche, C.; Prieto, C.; Fernández, A.I.; Cabeza, L.F. Review of reactors with potential use in thermochemical energy storage in concentrated solar power plants. *Energies* **2018**, *11*, 2358. [CrossRef]
12. Wokon, M.; Kohzer, A.; Linder, M. Investigations on thermochemical energy storage based on technical grade manganese-iron oxide in a lab-scale packed bed reactor. *Sol. Energy* **2017**, *153*, 200–214. [CrossRef]
13. Dreißigacker, V.; Zunft, S.; Müller-Steinhagen, H. A thermo-mechanical model of packed-bed storage and experimental validation. *Appl. Energy* **2013**, *111*, 1120–1125. [CrossRef]
14. Zhang, Y.N.; Wang, R.Z.; Li, T.X. Experimental investigation on an open sorption thermal storage system for space heating. *Energy* **2017**, *141*, 2421–2433. [CrossRef]
15. Clark, R.J.; Farid, M. Experimental investigation into the performance of novel $SrCl_2$-based composite material for thermochemical energy storage. *J. Energy Storage* **2021**, *36*, 102390. [CrossRef]
16. Courbon, E.; D'Ans, P.; Skrylnyk, O.; Frère, M. New prominent lithium bromide-based composites for thermal energy storage. *J. Energy Storage* **2020**, *32*, 101699. [CrossRef]
17. Bérut, E.; Bois, L.; Touloumet, Q.; Outin, J.; Ondarts, M.; Postole, G.; López, M.J.R.; Auroux, A.; Le Pierrès, N. Characterization of silica-PEG-$CaCl_2$ composite sorbents in an open thermochemical heat storage reactor. *J. Energy Storage* **2023**, *72*, 108632. [CrossRef]
18. Gbenou, T.R.S.; Fopah-Lele, A.; Wang, K. Macroscopic and microscopic investigations of low-temperature thermochemical heat storage reactors: A review. *Renew. Sustain. Energy Rev.* **2022**, *161*, 112152. [CrossRef]
19. Liu, H.; Nagano, K.; Sugiyama, D.; Togawa, J.; Nakamura, M. Honeycomb filters made from mesoporous composite material for an open sorption thermal energy storage system to store low-temperature industrial waste heat. *Int. J. Heat Mass Transf.* **2013**, *65*, 471–480. [CrossRef]
20. Van Essen, V.M.; Gores, J.C.; Bleijendaal, L.P.J.; Zondag, H.A.; Schuitema, R.; Bakker, M.; van Helden, W.G.J. Characterization of salt hydrates for compact seasonal thermochemical storage. In Proceedings of the ASME 3rd International Conference on Energy Sustainability 2009, ES2009, San Francisco, CA, USA, 19–23 July 2009. [CrossRef]
21. Clark, R.J.; Gholamibozanjani, G.; Woods, J.; Kaur, S.; Odukomaiya, A.; Al-Hallaj, S.; Farid, M. Experimental screening of salt hydrates for thermochemical energy storage for building heating application. *J. Energy Storage* **2022**, *51*, 104415. [CrossRef]
22. N'Tsoukpoe, K.E.; Schmidt, T.; Rammelberg, H.U.; Watts, B.A.; Ruck, W.K.L. A systematic multi-step screening of numerous salt hydrates for low temperature thermochemical energy storage. *Appl. Energy* **2014**, *124*, 1–16. [CrossRef]
23. Courbon, E.; D'Ans, P.; Permyakova, A.; Skrylnyk, O.; Steunou, N.; Degrez, M.; Frère, M. A new composite sorbent based on SrBr2 and silica gel for solar energy storage application with high energy storage density and stability. *Appl. Energy* **2017**, *190*, 1184–1194. [CrossRef]
24. Mills, A.; Farid, M.; Selman, J.R.; Al-Hallaj, S. Thermal conductivity enhancement of phase change materials using a graphite matrix. *Appl. Therm. Eng.* **2006**, *26*, 1652–1661. [CrossRef]
25. Barreneche, C.; Fernández, A.I.; Cabeza, L.F.; Cuypers, R. Thermophysical characterization and thermal cycling stability of two TCM: $CaCl_2$ and zeolite. *Appl. Energy* **2015**, *137*, 726–730. [CrossRef]
26. Donkers, P.A.J.; Adan, O.C.G.; Smeulders, D.M.J. Hydration/Dehydration Processes in Stabilized $CaCl_2$. In Proceedings of the 6th Biot Conference on Poromechanics, Paris, France, 9–13 July 2017. [CrossRef]
27. Restuccia, G.; Freni, A.; Vasta, S.; Aristov, Y. Selective water sorbent for solid sorption chiller: Experimental results and modelling. *Int. J. Refrig.* **2004**, *27*, 284–293. [CrossRef]
28. Iyimen-Schwarz, Z.; Lechner, M.D. Energiespeicherung durch chemische reaktionen. I. DSC-messungen zur quantitativen verfolgung der enthalpieänderungen von speicherstoffen für die hin- und rückreaktion. *Thermochim. Acta* **1983**, *68*, 349–361. [CrossRef]
29. Lemmon, E.W.; Jacobsen, R.T.; Penoncello, S.G.; Friend, D.G. Thermodynamic properties of air and mixtures of nitrogen, argon, and oxygen from 60 to 2000 K at pressures to 2000 MPa. *J. Phys. Chem. Ref. Data* **2000**, *29*, 331–385. [CrossRef]
30. Dinçer, İ.; Zamfirescu, C. *Drying Phenomena: Theory and Applications*; John Wiley & Sons, Ltd.: Hoboken, NJ, USA, 2015. [CrossRef]
31. Miao, Q.; Zhang, Y.; Jia, X.; Tan, L.; Ding, Y. $MgSO_4$-expanded graphite composites for mass and heat transfer enhancement of thermochemical energy storage. *Solar Energy* **2021**, *220*, 432–439. [CrossRef]
32. Xu, C.; Yu, Z.; Xie, Y.; Ren, Y.; Ye, F.; Ju, X. Study of the hydration behavior of zeolite-$MgSO_4$ composites for long-term heat storage. *Appl. Therm. Eng.* **2018**, *129*, 250–259. [CrossRef]
33. Michel, B.; Mazet, N.; Neveu, P. Experimental investigation of an innovative thermochemical process operating with a hydrate salt and moist air for thermal storage of solar energy: Global performance. *Appl. Energy* **2014**, *129*, 177–186. [CrossRef]

34. Molenda, M.; Stengler, J.; Linder, M.; Wörner, A. Reversible hydration behavior of $CaCl_2$ at high H_2O partial pressures for thermochemical energy storage. *Thermochim. Acta* **2013**, *560*, 76–81. [CrossRef]
35. Farcot, L.; Le Pierrès, N.; Michel, B.; Fourmigué, J.F.; Papillon, P. Numerical investigations of a continuous thermochemical heat storage reactor. *J. Energy Storage* **2018**, *20*, 109–119. [CrossRef]
36. Clark, R.J.; Farid, M. Hydration reaction kinetics of $SrCl_2$ and $SrCl_2$-cement composite material for thermochemical energy storage. *Sol. Energy Mater. Sol. Cells* **2021**, *231*, 111311. [CrossRef]
37. Sögütoglu, L.C.; Birkelbach, F.; Werner, A.; Fischer, H.; Huinink, H.; Adan, O. Hydration of salts as a two-step process: Water adsorption and hydrate formation. *Thermochim. Acta* **2021**, *695*, 178819. [CrossRef]
38. Chen, B.; Johannes, K.; Horgnies, M.; Morin, V.; Kuznik, F. Characterization of an ettringite-based thermochemical energy storage material in an open-mode reactor. *J. Energy Storage* **2021**, *33*, 102159. [CrossRef]
39. Clark, R.J.; Farid, M. Experimental investigation into cascade thermochemical energy storage system using $SrCl_2$-cement and zeolite-13X materials. *Appl. Energy* **2022**, *316*, 119145. [CrossRef]